



UNIVERSITY OF LEEDS

This is a repository copy of *Forced Gravity Waves and the Tropospheric Response to Convection*.

White Rose Research Online URL for this paper:
<http://eprints.whiterose.ac.uk/128507/>

Version: Accepted Version

Article:

Halliday, OJ orcid.org/0000-0002-8863-9081, Griffiths, SD
orcid.org/0000-0002-4654-2636, Parker, DJ orcid.org/0000-0003-2335-8198 et al. (2 more authors) (2018) *Forced Gravity Waves and the Tropospheric Response to Convection*. Quarterly Journal of the Royal Meteorological Society, 144 (712). Part A. pp. 917-933. ISSN 0035-9009

<https://doi.org/10.1002/qj.3278>

Reuse

Items deposited in White Rose Research Online are protected by copyright, with all rights reserved unless indicated otherwise. They may be downloaded and/or printed for private study, or other acts as permitted by national copyright laws. The publisher or other rights holders may allow further reproduction and re-use of the full text version. This is indicated by the licence information on the White Rose Research Online record for the item.

Takedown

If you consider content in White Rose Research Online to be in breach of UK law, please notify us by emailing eprints@whiterose.ac.uk including the URL of the record and the reason for the withdrawal request.



eprints@whiterose.ac.uk
<https://eprints.whiterose.ac.uk/>



Forced Gravity Waves and the Tropospheric Response to Convection

Oliver J. Halliday^{a*}, Stephen D. Griffiths^b, Douglas J. Parker^a, Alison Stirling^c and Simon Vosper^c

^a*Institute for Climate and Atmospheric Science, School of Earth and Environment, University of Leeds, UK*

^b*Department of Applied Mathematics, University of Leeds, UK*

^c*Met Office, UK*

*Correspondence to: O. J. Halliday, Institute for Climate and Atmospheric Science, University of Leeds, Leeds, LS2 9JT. E-mail:

mm10ojh@leeds.ac.uk

We present theoretical work directed toward improving our understanding of the mesoscale influence of deep convection on its tropospheric environment through forced gravity waves. From the linear, hydrostatic, non-rotating, incompressible equations, we find a two-dimensional analytical solution to prescribed heating in a stratified atmosphere, which is upwardly radiating from the troposphere when the domain lid is sufficiently high. We interrogate the spatial and temporal sensitivity of both the vertical velocity and potential temperature to different heating functions, considering both the near-field and remote responses to steady and pulsed heating. We find that the mesoscale tropospheric response to convection is significantly dependent on the upward radiation characteristics of the gravity waves, which are in turn dependent upon the temporal and spatial structure of the source, and the assumed stratification. We find a 50% reduction in troposphericly averaged vertical velocity when moving from a trapped (i.e. low lid) to upwardly-radiating (i.e. high lid) solution, but even with maximal upward radiation, we still observe significant tropospheric vertical velocities in the far-field 4 hours after heating ends. We quantify the errors associated with coarsening a 10 km wide heating to a 100 km grid (in the way a General Circulation Model (GCM) would), observing a 20% reduction in vertical velocity. The implications of these results for the parameterisation of convection in low-resolution numerical models are quantified and it is shown that the smoothing of heating over a grid-box leads to significant in grid-box tendencies, due to the erroneous rate of transfer of compensating subsidence to neighbouring regions. Further, we explore a simple time-dependent heating parameterisation that minimises error in a parent GCM grid box, albeit at the expense of increased error in the neighbourhood.

1. Introduction

Tropical deep convection is observed to be organised on the synoptic and mesoscale (Wheeler and Kiladis 1999; Tulich et al. 2007), and it is argued that gravity waves provide a mechanism for the aggregation of cumulonimbus storms (Tulich et al. 2011) as they communicate the necessary atmospheric adjustment to the neighbouring troposphere through subsidence or lifting. The “gregarious” nature of mesoscale tropical convection cells is thought to be driven (at least in part) by a low-level rising mode in the vicinity of a convecting storm, which increases the depth of moisture at low-levels, making conditions more favourable for new convective events (Mapes 1993; Fovell et al. 1992). Momentum and temperature changes, communicated through the propagation of convectively generated gravity waves may also condition the remote troposphere to convection triggering or suppression (Bretherton and Smolarkiewicz 1989; Pandya et al. 2000; Shige and Satomura 2000).

In current General Circulation Models (GCMs) deep convection is represented as a sub-grid process, and so a theoretical understanding of the way in which convective heating gives rise to tropospheric adjustment is essential. A sub-grid convection scheme adjusts the temperature, moisture and cloud fields within a grid column, leaving the resolved dynamics to propagate this adjustment more remotely, and thus influencing the convective available potential energy (CAPE) of the wider environment (Stensrud 2009). Therefore, the dynamical response to convection is highly dependent upon the model convection scheme, which itself is sensitive to the closures and assumptions placed upon the parameterisations. There are a number of types of deep convective parameterisation scheme in operational use (Stensrud 2009). Typically, a convection scheme attempts to represent an ensemble of clouds within a given gridbox through a bulk formulation. For instance the Gregory and Rowntree mass-flux scheme used in the MetUM (Gregory and Rowntree 1990; Walters et al. 2017) models the effects of entrainment and detrainment on the ensemble convective-cloud mass flux through analogy with a single plume in the gridbox. The resulting tendencies are applied at the grid scale, and it is assumed that all compensating subsidence occurs within that gridbox (in reality it has long been known that

gravity waves propagate laterally to move the zones of subsidence away from the location of the forcing, e.g. Yanai et al. 1973). While gravity-wave modes are themselves represented only by the resolved grid, representation of the *drag* caused by gravity-wave breaking, and initiated by sub-grid orography (and sometimes precipitating convection) is parametrised separately (e.g. Walters et al. 2017, Bushell et al. 2015). Some sub-grid statistics of the cloud field are diagnosed in the model (via the Prognostic Cloud Scheme), but these are principally used to interact with the radiation scheme and do not feed back on to the dynamic, thermodynamic and cloud fields at present.

In summary, while current convection schemes hold some information about the subgrid cloud field, they do not use any subgrid cloud information in the excitation of gravity waves: waves are only forced by the grid-resolved tendencies imposed by the convection scheme. This leads to a possible mis-match between the true field of gravity waves excited by subgrid convection on the kilometre scale and the gravity waves forced on the grid scale by the convection scheme. It is still an open question whether such effects need to be handled explicitly in convection schemes, or whether the model grid will handle them satisfactorily.

Gravity waves modify the troposphere through vertical motion. If the vertical motion at low levels is strong, of the order of metres per second as may occur in a trapped gravity wave or bore, then this may directly trigger deep convection (Emanuel et al. 1994). However, even relatively weak vertical motion on the order of centimetres per second will induce adiabatic warming and cooling that modifies the stability of the atmospheric profile, through its CAPE and convective inhibition (CIN). A number of case studies focus upon tropospheric gravity waves’ initiation and/or control of the initiation of convection at locations remote from the parent storm (Zhang et al. 2001; Lac et al. 2002; Hankinson et al. 2014). In particular, gravity waves have been observed to suppress the second initiation of convection through waves of subsidence for up to six hours after initial forcing, until waves of low-level ascent removes the inhibition and allows the convection to occur (Marshall and Parker 2006; Birch et al. 2013).

In any such study, there is an open question of whether the strength of the gravity wave signal in the far field from the source

is dependent on trapping of the waves within the troposphere. For example Lindzen and Tung (1976) showed that a change in stability at the tropopause plays a part in the formation of deep tropospheric gravity wave modes as waves will be partially reflected due to the sudden change in stability. The trapping conditions can be non-trivial to diagnose on a case by case basis. Conditions of trapping could be met for certain ranges of horizontal wavenumber if there are suitable patterns of wind profile and stratification (Birch et al. 2013), and when trapping occurs, a rigid lid model may be suitable to analyse the wave field. More generally a radiative boundary condition located at the tropopause is, physically, more realistic than a rigid lid but it is mathematically disruptive (Edman and Romps 2017). Certainly, such a condition does not lend itself to an analytical treatment of forced convection. However, previous theoretical studies have shown that one can circumvent this difficulty with a high rigid lid (Nicholls et al. 1991; Mapes 1998; Holton et al. 2002) and still retain wave-like structures in the troposphere. Nicholls et al. constructed a restricted, idealised semi-analytical model using a Dirichlet rigid lid condition, the location of which is raised aloft, to address the influence of vertical gravity waves in adjusting the neighbouring cloud-free troposphere. The importance of mode 1 and 2 gravity waves is apparent in their results and confirmed by Lane and Reeder (2011), who show that the mode 3 gravity wave also plays a significant role in modifying convective inhibition in the neighbourhood of deep convection. Here, we extend the work of Nicholls et al. (1991) by i) using a projection technique to find an analytical solution to a semi-infinite atmosphere with a simple stratification, while ii) removing the Boussinesq assumption and thus allowing for a deep atmosphere, and iii) allowing for a jump in the buoyancy frequency, to include the effects of a model stratosphere.

A number of idealised studies (Lindzen 1974; Raymond 1983; Emanuel 1986) have interrogated the interaction and self-organisation between tropospheric gravity waves and deep convection but these authors have been unable to obtain realistic wave propagation speeds and leave questions on the significance of wave trapping and the sensitivity to the convective forcing unanswered. Whilst a number of numerical models have improved our understanding of the way in which convection is coupled to

gravity waves (Lane and Zhang 2011; Lane et al. 2001; Holton and Alexander 1999; Piani et al. 2000; Tulich and Mapes 2008), the fact that existent parameterisation schemes' capture of the spatial and temporal distribution of cumulonimbus storms is unsatisfactory is a clear indicator that current understanding is deficient (Stephens et al. 2010). Whilst this may be attributable to other, omitted physical processes and feedbacks, an improved representation of gravity wave-cloud interactions also provides a candidate hypothesis worthy of deeper investigation.

The Earth's rotation also affects the tropospheric response to deep convection: the gravity waves are part of a Rossby adjustment to the convection, and their propagation establishes a larger-scale balanced response to the potential vorticity field created by the convective sources. Inclusion of planetary rotation also significantly increases the complexity of the problem, by perturbing the gravity wave dispersion relation, making mathematically tractable gravity wave modes illusive. Numerical studies that have examined isolated clouds in rotating frames (Shutts and Gray 1994; Andersen and Kuang 2008) do indicate that the Coriolis force is important in reducing the radius of influence of the wave modes (Liu and Moncrieff 2004). We reserve for a later publication a consideration of Coriolis effects.

Here, based on an analytical description of a deep atmosphere which is thermally forced via a prescribed heating function, we build a model capable of addressing two questions:

1. How does the proportion of upward-wave radiation affect the spatial and temporal distribution of convective adjustment over the timescales of a few hours, relevant to mesoscale dynamics?
2. How does the spatial and temporal distribution of convective forcing affect the gravity-wave characteristics?

In this article, we extend the analytical work of Nicholls et al. (1991), Holton et al. (2002) and Edman and Romps (2017) to address the above questions, assessing the mesoscale effect of horizontal and vertical variation in the pattern of convective forcing, with special attention paid to the sensitivity of the remote horizontal response, as well as atmospheric stratification. Specifically, we develop and apply a suitable analytical model that accommodates variation in both the spatial and temporal

patterning of thermal forcing. To facilitate an analytical study, we will base our model on idealised, linear equations for a deep atmosphere and generalise a technique due to Nicholls et al. (1991) in which the upper boundary or lid of the domain is many times higher aloft than the tropopause, so that the solution asymptotes to what can be considered a pseudo-radiating regime. As in those previous studies, we choose two-dimensional planar geometry in an environment without vertical shear. The importance of shear in squall line development has been shown by Thorpe et al. (1982), Rotunno et al. (1988) and Schmidt et al. (1990), but studies have confirmed it is not necessary in all cases (Barnes and Sieckman 1984), and a symmetrical response can even be found in simulations with complicated environmental wind (Nicholls 1987). Furthermore, real deep convection also occurs in highly curved geometries, and there are a number of interesting studies tackling aspects of this problem by utilising fully 3D numerical simulations with complex physics. In such simulations, more realistic physical features, such as typhoon generated gravity waves (Kim and Chun 2011; Kim et al. 2014; Ong et al. 2017), mesoscale circulation around squall lines (Pandya et al. 2000), and gravity waves generated by deep convection (Piani et al. 2000; Lane and Reeder 2001) can be modelled. Two-dimensional planar geometry in the absence of shear (which achieves wave reflection/refraction through a change in stratification) is chosen here as the simplest model with which we can confront the above questions.

We organise as follows. Section 2 develops a two dimensional, analytical model for thermally forced response in the troposphere, relying on a rigid-lid Dirichlet boundary condition, then considers its convergence onto a radiating solution as its lid is raised aloft. Sections 3 & 4 compare results from three model regimes: i) trapped solutions, ii) radiating solutions with constant buoyancy frequency and iii) radiating solutions with piecewise constant buoyancy frequency, separated at the tropopause. In Section 3 we focus on the near and far field dynamical response to both transient and steady heat forcing. In section 4 we quantify the error associated with coarsening a forcing to a grid that does not explicitly resolve the heating. Section 5 will present conclusions.

2. Mathematical Model

2.1. Governing equations

We consider small disturbances about a state of rest, in a two-dimensional incompressible fluid. The governing equations for hydrostatic flow are

$$\begin{aligned} \frac{\partial u}{\partial t} &= -\frac{1}{\rho_0(z)} \frac{\partial p'}{\partial x}, & \frac{1}{\rho_0(z)} \frac{\partial p'}{\partial z} &= b, \\ \frac{\partial b}{\partial t} + N^2 w &= S, & \frac{\partial u}{\partial x} + \frac{\partial w}{\partial z} &= 0, \end{aligned} \quad (1)$$

where (u, w) is the wind vector, p' is the perturbation pressure, $\rho_0(z)$ is the basic state density, $b = -g\rho'/\rho_0(z)$ is the buoyancy (where ρ' is the perturbation density), $S(x, z, t)$ is a prescribed buoyancy forcing, and $N(z)$ is the buoyancy frequency, defined by

$$N^2(z) = -\frac{g}{\rho_0(z)} \frac{d\rho_0(z)}{dz}. \quad (2)$$

We do not make the Boussinesq approximation, i.e., ρ_0 is not taken to be constant in the horizontal momentum equation, so that the effects of a deep (albeit incompressible) atmosphere are included. (e.g., see §6.4 of Gill (1982). This is a widely-used system of equations in dynamical meteorology (e.g., Lindzen (1974), Chumakova et al. (2013))

The buoyancy forcing S , with units of m s^{-3} , arises due to a thermal forcing Q , with units of K s^{-1} , which in a more complete description would appear in the potential temperature equation $D\theta/Dt = Q$. We use a Boussinesq-like correspondence between the two, with

$$S = \frac{gQ}{\theta_0}, \quad (3)$$

where θ_0 is a reference potential temperature (taken to be 273 K). Later on, we will also evaluate a potential temperature perturbation θ' from b , again using a Boussinesq-like correspondence

$$b = \frac{g\theta'}{\theta_0}. \quad (4)$$

Eliminating variables in (1), a single equation for the vertical velocity w may be obtained in terms of S :

$$\frac{\partial}{\partial z} \left(\rho_0(z) \frac{\partial}{\partial z} \frac{\partial^2 w}{\partial t^2} \right) + \rho_0(z) N^2(z) \frac{\partial^2 w}{\partial x^2} = \rho_0(z) \frac{\partial^2 S}{\partial x^2}. \quad (5)$$

This is to be solved between rigid lower and upper boundaries at $z = 0$ and $z = H$:

$$w(z = 0) = 0, \quad w(z = H) = 0. \quad (6)$$

2.2. Modal Expansion

Free modes of the form $w = A(x - c_n t)\phi_n(z)$, with horizontal wave speed c_n , satisfy (5) and (6) provided

$$\begin{aligned} \frac{d}{dz} \left(\rho_0 \frac{d\phi_n}{dz} \right) + \frac{\rho_0 N^2}{c_n^2} \phi_n &= 0, \\ \phi_n(0) = \phi_n(H) &= 0, \end{aligned} \quad (7)$$

where $\rho_0(z)$ and $N(z)$ are linked via (2). From (7), it follows that the eigenvalues c_n are real, and that the eigenfunctions $\phi_n(z)$ satisfy an orthonormality condition:

$$\int_0^H \rho_0 N^2 \phi_n \phi_m dz = \delta_{nm}. \quad (8)$$

Since the eigenfunctions, $\phi_n(z)$, are complete, the vertical structure of $w(x, z, t)$ and $S(x, z, t)$ can be written as

$$\begin{aligned} w(x, z, t) &= \sum_{j=1}^{\infty} w_j(x, t) \phi_j(z), \\ S(x, z, t) &= N^2(z) \sum_{j=1}^{\infty} S_j(x, t) \phi_j(z). \end{aligned} \quad (9)$$

The inclusion of the pre-factor $N^2(z)$ in S is for mathematical convenience, so that when multiplied by $\rho_0 \phi_n$ and integrated over $0 < z < H$ we obtain

$$S_n(x, t) = \int_0^H \rho_0(z) \phi_n(z) S(x, z, t) dz, \quad (10)$$

i.e. $S_n(x, t)$ is completely determined by the given buoyancy forcing $S(x, z, t)$. However, the modal expansion coefficients $w_n(x, t)$ must be found from evolution equations, which are obtained by multiplying (5) by ϕ_n and integrating over $0 < z < H$ yielding

$$\begin{aligned} -\frac{1}{c_n^2} \int_0^H \rho_0 N^2 \phi_n \frac{\partial^2 w}{\partial t^2} dz + \int_0^H \rho_0 N^2 \phi_n \frac{\partial^2 w}{\partial x^2} dz \\ = \int_0^H \rho_0 \phi_n \frac{\partial^2 S}{\partial x^2} dz, \end{aligned} \quad (11)$$

where the first term has been twice integrated by parts, and we have used (7). Substituting the modal expansions (9) and using (8) we obtain

$$\frac{\partial^2}{\partial x^2} w_n(x, t) - \frac{1}{c_n^2} \frac{\partial^2}{\partial t^2} w_n(x, t) = \frac{\partial^2}{\partial x^2} S_n(x, t), \quad (12)$$

which, for $S = 0$ simplifies to the second order wave equation, for free modes of horizontal speed c_n .

Equation (12) is the basis for the rest of this study. Once solved, we shall find the full solutions for $w(x, z, t)$ from (9) and for $b(x, z, t)$ by integrating $\partial b / \partial t = S - N^2 w$.

2.3. Buoyancy forcing: temporal structure

We assume a separable buoyancy forcing of finite duration, T :

$$S(x, z, t) = S_0 X(x) Z(z) (\Theta(t) - \Theta(t - T)), \quad T > 0. \quad (13)$$

Here $Z(z)$ and $X(x)$ are vertical and horizontal structure functions with maximum amplitude unity, $\Theta(t)$ is the Heaviside function, and S_0 is the maximum value of the buoyancy forcing. Then (12) becomes

$$\frac{\partial^2 w_n}{\partial x^2} - \frac{1}{c_n^2} \frac{\partial^2 w_n}{\partial t^2} = S_0 \sigma_n \frac{\partial^2 X}{\partial x^2} (\Theta(t) - \Theta(t - T)),$$

where

$$\sigma_n = \int_0^H \rho_0(z) \phi_n(z) Z(z) dz. \quad (14)$$

This may be solved, for arbitrary $X(x)$, using a Fourier transform in x (with conjugate variable k) and a Laplace transform in t (with conjugate variable p), following Nicholls et al. (1991). Using standard transform relations (e.g., Arfken 2013) we obtain

$$\tilde{w}_n(k, p) = \frac{S_0 c_n^2 \sigma_n k^2 \tilde{X}(k)}{p(p + i c_n k)(p - i c_n k)} (1 - e^{-pT}). \quad (15)$$

Here \tilde{X} denotes the Fourier transform of $X(x)$, and \tilde{w} the Fourier and Laplace transform of w . The above result assumes quiescent initial conditions, and that $w \rightarrow 0$ as $|x| \rightarrow \infty$ sufficiently quickly for the Fourier transform to exist.

Using the delay theorem of Laplace transforms (e.g., Arfken 2013) on the partial fraction expansion of (15), taking inverse

Laplace and Fourier transforms yields

$$\begin{aligned}
 w_n(x, t) = & S_0 (1 - \Theta(t - T)) X(x) \sigma_n \\
 & - \frac{S_0}{2} (X(x + c_n t) + X(x - c_n t)) \sigma_n \\
 & + \frac{S_0}{2} \Theta(t - T) (X(x - c_n(t - T))) \sigma_n \\
 & + \frac{S_0}{2} \Theta(t - T) (X(x + c_n(t - T))) \sigma_n. \quad (16)
 \end{aligned}$$

A few remarks are now appropriate. As in Nicholls et al. (1991) and Parker and Burton (2002), the modal solution contains nondispersive waves moving leftwards and rightwards with speed c_n . Also note (16) holds for any buoyancy forcing for which the horizontal and vertical structure is separable, and for any stratification; the response to steady buoyancy forcing may be obtained on setting $T \rightarrow \infty$, when terms with factor $\Theta(t - T)$ disappear.

The full vertical velocity, $w(x, z, t)$, can be determined from (16) when used with (9). The corresponding buoyancy response, $b(x, z, t)$, is obtained by substituting (16) and (9) into (1), to give

$$\begin{aligned}
 \frac{\partial}{\partial t} \left(\frac{b}{S_0} \right) = & \frac{N^2}{2} \Theta(t) \sum_n \sigma_n (X(x + c_n t) + X(x - c_n t)) \phi_n(z) \\
 & - \frac{N^2}{2} \Theta(t - T) \sum_n \sigma_n (X(\xi - c_n t) + X(\xi' + c_n t)) \phi_n(z), \quad (17)
 \end{aligned}$$

where, for convenience, we have defined $\xi = x + c_n T$, $\xi' = x - c_n T$.

2.4. Buoyancy forcing: spatial structure

To obtain quantitative predictions of w and b (and hence θ) a horizontal variation $X(x)$ and a vertical variation $Z(z)$ must be chosen. For $X(x)$ we choose a Gaussian function of horizontal width L :

$$X(x) = \exp\left(-\frac{x^2}{2L^2}\right), \quad (18)$$

since in localised deep convection the horizontal variation of buoyancy peaks at the hot-tower centre and weakens, due to, e.g., turbulent mixing with distance. The choice of $Z(z)$ is informed by observed heating profiles, which peak in the mid troposphere and are small at the surface and tropopause due to low-level cooling and the cessation of convective instability respectively. As

in Nicholls et al. (1991), a suitable first approximation is

$$Z(z) = \sin\left(\frac{\pi z}{H_t}\right) (\Theta(z) - \Theta(z - H_t)), \quad (19)$$

which is continuous and has a single peak at $z = H_t/2$, where H_t is the tropopause. Note, the tropopause now coincides with the top of the buoyancy forcing used throughout this article, i.e., $Z(z) = 0$ when $z > H_t$. Figure 1 is a schematic representation of the horizontal and vertical variation of the buoyancy forcing function we use throughout, except for section 4.2 (which we shall address at that time).

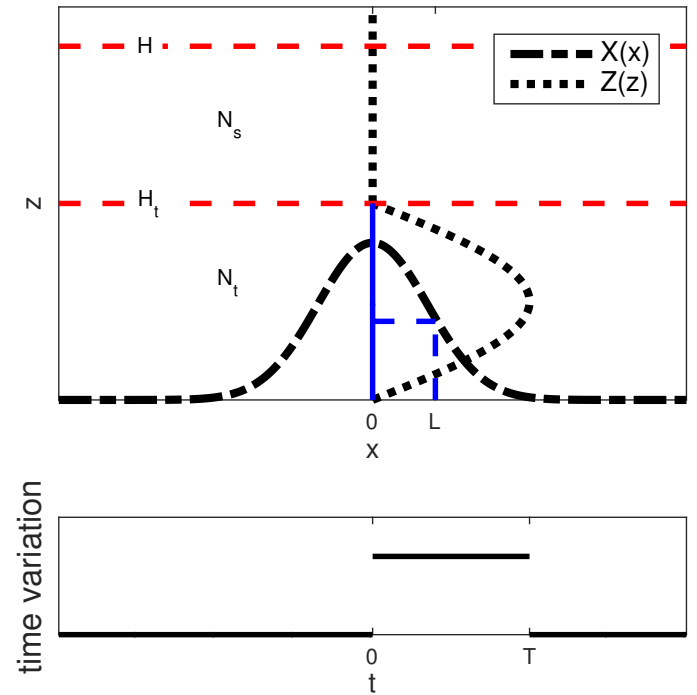


Figure 1. Schematic of the horizontal and vertical variation of our buoyancy forcing function. The top panel shows the vertical and horizontal variation described by $Z(z)$, $X(x)$, respectively. The characteristic width of the forcing is L . The bottom panel shows the time dependence. The vertical variation chosen corresponds to the first baroclinic mode of heating in the troposphere, between the ground and the tropopause (broken red line).

With this assumed form for X , the vertical velocity may be determined straightforwardly from (9) and (16). We may also now integrate (17), using the initial condition $b = 0$, to obtain

$$\begin{aligned}
 b = & S_0 \frac{N^2 L}{2} \sqrt{\frac{\pi}{2}} \sum_j \frac{\sigma_j}{c_j} \phi_j(z) \\
 & \times \{ \Theta(t) G(c_j, L, x, t) + \Theta(t - T) G(c_j, L, x, t - T) \}, \quad (20)
 \end{aligned}$$

where we have defined

$$G(c_j, L, x, t) = \operatorname{erf}\left(\frac{c_j t - x}{\sqrt{2}L}\right) + \operatorname{erf}\left(\frac{c_j t + x}{\sqrt{2}L}\right). \quad (21)$$

The potential temperature immediately follows from (4).

2.5. Model Stratification

The simplest possible representation of the tropospheric and stratospheric stratification is

$$N(z) = \begin{cases} N_t, & z \leq H_t, \\ N_s, & H > z > H_t, \end{cases} \quad (22)$$

which corresponds to a basic state of density of

$$\rho_0(z) = \begin{cases} \rho_s e^{-\frac{z}{D_t}}, & z \leq H_t, \\ \rho_s e^{-\frac{H_t}{D_t}} e^{-\frac{(z-H_t)}{D_s}}, & H > z > H_t. \end{cases} \quad (23)$$

For definiteness, let $N_s \geq N_t$. The tropospheric and stratospheric scale heights are given by

$$D_t = \frac{g}{N_t^2}, \quad D_s = \frac{g}{N_s^2}. \quad (24)$$

We seek the corresponding free modes $\phi_n(z)$ and wavespeeds c_n from (7), which yields a solution

$$\phi_n(z) = A_n \sin(k_n z) e^{\frac{z}{2D_t}}, \quad z < H_t, \quad (25)$$

$$\phi_n(z) = A'_n \sin(k'_n(z - H)) e^{\frac{z}{2D_s}}, \quad H_t \leq z < H, \quad (26)$$

where we have defined

$$k_n = \sqrt{\frac{N_t^2}{c_n^2} - \frac{1}{4D_t^2}}, \quad k'_n = \sqrt{\frac{N_s^2}{c_n^2} - \frac{1}{4D_s^2}}. \quad (27)$$

The solutions (25) and (26) must be matched at the tropopause, $z = H_t$, by applying continuity of ϕ_n and $d\phi_n/dz$, yielding an equation for c_n :

$$\frac{k_n}{k'_n} + \left(\frac{1}{D_t} - \frac{1}{D_s} \right) \frac{\tan(k_n H_t)}{k'_n} - \tan(k_n H_t) \cot(k'_n(H_t - H)) = 0. \quad (28)$$

We solved (28) numerically, using a bisection method, to determine seeding values of c_n which were then refined using a Newton-Raphson method. Recall that the wave speeds, c_n , are real.

Let us consider limiting cases. If $N_t = N_s \equiv N$, then (28) becomes $1 = \tan(k_n H_t) \cot(k(H_t - H)) \implies \tan(k_n H) (1 + \tan^2(k_n H_t)) = 0$, which gives $Hk_n = n\pi$, and from (27) we obtain for the wave speeds

$$c_n = \frac{NH}{\sqrt{n^2\pi^2 + \frac{H^2}{4D_t^2}}}. \quad (29)$$

The wavespeeds of Nicholls et al. (1991) are recovered in the Boussinesq limit, $H \ll D_t$, with $c_n \rightarrow NH/n\pi$, corresponding to Fourier modes $\phi_n(z) \rightarrow A_n \sin(n\pi z/H)$. The wavespeeds of Parker and Burton (2002) are recovered by further setting $H = H_t$. Returning to $N_t \neq N_s$, from (8) the normalization coefficients in (25) and (26) are

$$\begin{aligned} A_n &= \left(\frac{N_t^2 \rho_s}{2} \left(H_t - \frac{\sin(2k_n H_t)}{2k_n} \right) + \frac{N_s^2 \rho_s}{2} \left(\frac{\sin^2(k_n H_t)}{\sin^2(k'_n(H_t - H))} \right) \right. \\ &\quad \left. \times \left(H - H_t + \frac{\sin(2k'_n(H_t - H))}{2k'_n} \right) \right)^{1/2}, \quad (30) \\ A'_n &= \left(\frac{\sin(k_n H_t)}{\sin(k'_n(H_t - H))} \right) \\ &\quad \times \exp \left(\left(\frac{1}{2D_t} - \frac{1}{2D_s} \right) H_t \right) A_n. \end{aligned}$$

From (14), with our choice $Z(z) = \sin(\pi z/H_t) (\Theta(z) - \Theta(z - H_t))$ we now find

$$\sigma_n = \frac{\rho_s A_n}{2} \text{Re} \left(\frac{\exp(ik_n H_t - H_t/2H) + 1}{ik_n + i\frac{\pi}{H_t} - \frac{1}{2D_s}} - \frac{\exp(ik_n H_t - H_t/2H) + 1}{ik_n - i\frac{\pi}{H_t} - \frac{1}{2H_s}} \right), \quad (31)$$

with the A_n determined from (30), and the c_n and k_n via a numerical solution of (28).

2.6. Convergence to a Radiating Solution

The existence of a model lid at $z = H$ means that upwards propagating waves are inevitably reflected downwards, and will thus return to disrupt the tropospheric response in $0 < z < H_t$, in which we are most interested. This aphysical effect could perhaps be eliminated by taking $H \approx 50$ km and introducing a sponge layer at the top of the domain. However, a neater solution - and one which is compatible with our mathematical formulation - is

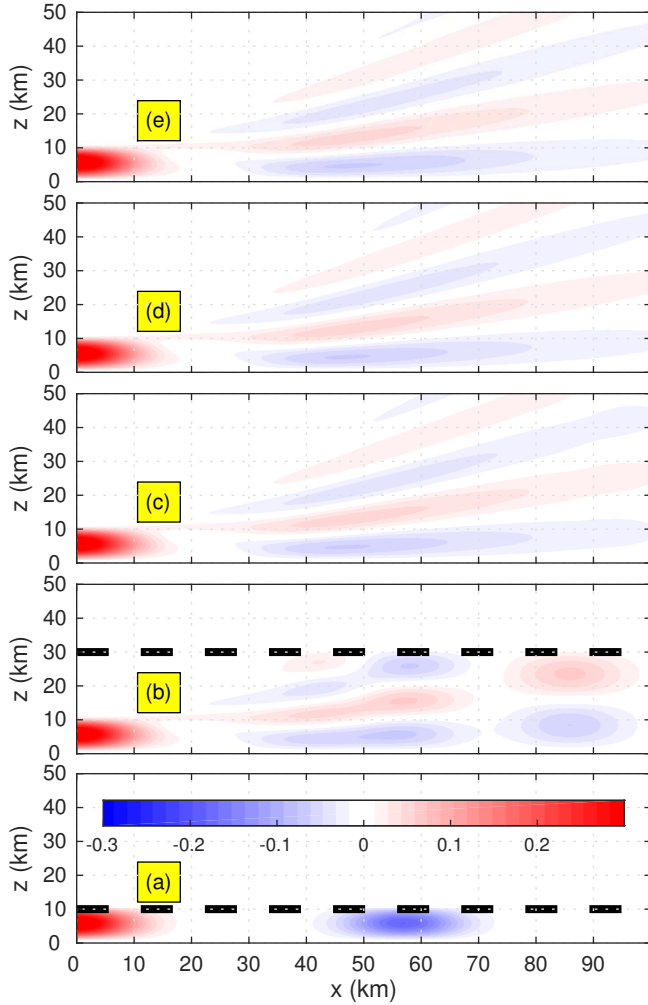


Figure 2. The transition to a radiating solution with increasing lid altitude $H \gg H_t = 10$ km. Shown is the w response for $x > 0$ in m s^{-1} , 30 mins after onset of forcing. $L = 10$ km, $N = 0.01 \text{ s}^{-1}$, $H_t = 10$ km. (a) $H = 10$ km, (b) $H = 30$ km, (c) $H = 100$ km, (d) $H = 640$ km, (e) $H = 3000$ km.

simply to take $H \gg H_t$, so that upwards propagating waves do not have time to reflect and return to disrupt the tropospheric response, which can then be considered as quasi-radiating. The values of H that are required to achieve this may themselves be aphysical (e.g., hundreds of km), in which case the response only makes sense physically in the troposphere and stratosphere (say). The response far above that, where our equations are motion are not valid, is ignored: this part of the domain simply serves to implement a radiating boundary condition for the lower atmosphere.

But how large need H be for such a quasi-radiating response? We probe the convergence of the tropospheric response as H increases for the case of a uniformly stratified atmosphere $N(z) = N = 0.01 \text{ s}^{-1}$ and with steady forcing such that $L = 10$ km, $H_t = 10$ km, which shall be the standard choice throughout. Figure 2 shows the w response for $x > 0$, 30 mins after forcing onset, for a lid at 10 km (tropopause), 30 km, 100 km, 640 km, 3000 km. We are thus moving from the trapped mode ($H = H_t$) of Parker and

Burton (2002), to a model with $H = 30$ km and limited upward radiation (Nicholls et al. 1991), and then eventually converging to radiating solution when $H \gg H_t$. In particular, we see large differences as H increases from 10 to 100 km: higher order modes (with larger horizontal phase speeds) are excited and propagate more rapidly into the environment, and an upwardly radiating gravity wave field develops aloft. However, increasing lid height above 100 km has almost no effect on tropospheric response, although the stratospheric response changes somewhat. Indeed, figure 2(d, e) are indistinguishable, which indicates a converged solution. This convergence is quantified using an absolute difference

$$\Delta w(x, z, t, H, L) = w(x, z, t, H, L) - w_\infty(x, z, t, L), \quad (32)$$

where w_∞ is the converged solution with $H = 3000$ km (figure 2(e)). We calculate the tropospheric relative error

$$\epsilon(H, L) = \frac{\Delta w_{rms}(x, z, t, H)}{(w_\infty)_{rms}}, \quad (33)$$

$$f_{rms} \equiv \sqrt{\frac{\sum_x \sum_z (f(x, z, t))^2}{N_x N_z}},$$

where the uniform grid on which a response f is evaluated contains $N_x \times N_z$ points, in the domain $0 < x < 300$ km, $0 < z < 10$ km. In figure 2, the calculated values of ϵ are, reading upwards, 1.06, 0.12, 8.5×10^{-4} , 2.3×10^{-12} (panel (e) is w_∞). Arbitrarily, we deem that a value of $\epsilon \leq 10^{-3}$ corresponds to a converged solution, and therefore figure 2(c,d) can be considered converged.

It is also important to consider how ϵ depends upon L . Figure 3 shows the convergence for a range of horizontal forcing widths $1 \text{ km} < L < 100$ km. We observe that, generally, when L is smaller, ϵ is larger. For the range of L used in this study, $10 \text{ km} \leq L \leq 100$ km, taking $H_t = 640$ km we are guaranteed $\epsilon \leq 10^{-3}$ (for this choice of parameter space). We therefore take this value of H for rest of this study.

We can understand the dependence of ϵ on L by considering hydrostatic gravity waves $\sim \exp\{i(kx + mz - \omega t)\}$ in an unbounded atmosphere with uniform N , taken here in the Boussinesq limit for simplicity. Taking this limit in (5), we obtain

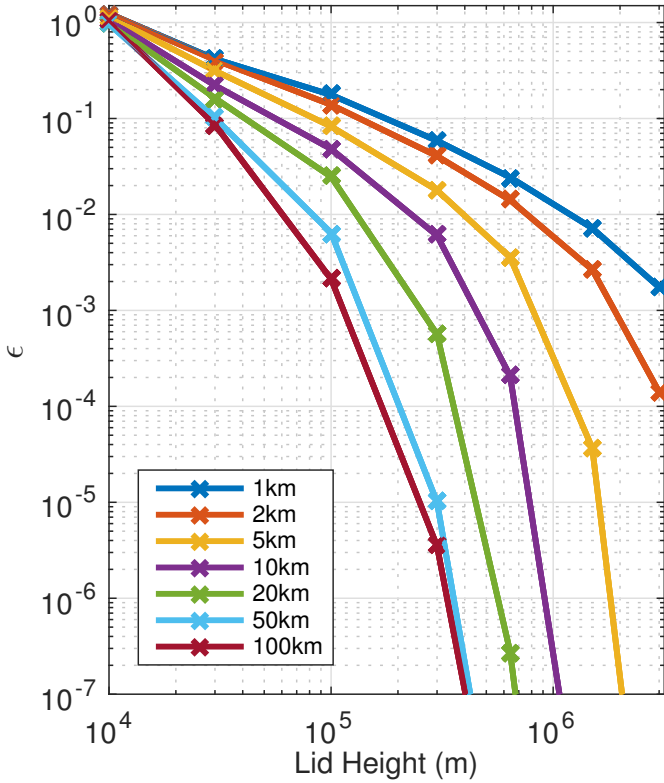


Figure 3. Convergence with H of the simplified (constant N) model. Plots of the relative error in the w -response, ϵ , with lid height, H , compiled for $t = 30$ mins after the onset of forcing, $0 < x < 300$ km and a range of forcing widths L : $1 \text{ km} < L < 100$ km (see key) with the same total heat input. As expected, horizontally narrower forcing profiles converge more slowly with H .

the usual gravity wave dispersion relation, $\omega = Nk/m$, and hence a group velocity

$$c_g = \left(\frac{\partial \omega}{\partial k}, 0, \frac{\partial \omega}{\partial m} \right) = \frac{N}{m} \left(1, 0, -\frac{k}{m} \right). \quad (34)$$

The time taken for wave energy to reflect from the lid and return

$$t_r = \frac{2H}{c_{gz}} = \frac{2H}{Nk/m^2} = \frac{2Hm^2}{Nk}. \quad (35)$$

Such unphysical reflections can then be avoided by taking $t < t_r$, or equivalently, $H > Nkt/2m^2$. Since we expect the gravity wave response to have the same characteristic scales as the forcing, i.e. $k \approx L^{-1}$ and $m \approx H_t^{-1}$, we require

$$H > \frac{NH_t^2 t}{2L}. \quad (36)$$

So, for a quasi-radiating solution at large t , we would need a large H . For our convergence tests with $t = 30$ mins, $N = 0.01 \text{ s}^{-1}$, $L = 10$ km and $H_t = 10$ km, we thus expect a converged solution with $H > 250$ km.

The number of modes M retained in the modal expansion also need to vary with H to ensure a consistent resolution of both the forcing and the response. We achieve this by taking $M = 20H/H_t$.

3. Results

We now test the sensitivity of the gravity wave response to different model configurations (e.g., constant versus varying N) and to the temporal and spatial structure of the thermal forcing. Of particular interest is the speed and magnitude of the resulting dominant tropospheric response, and how this may pre-condition the troposphere to further convection. We also identify aspects of the tropospheric response that may be absent in low-resolution atmospheric models. Throughout we analyse the vertical velocity w and the potential temperature perturbation θ , since both are influential in the organisation of deep convection.

We use results from three different model configurations: (i) a trapped regime with a rigid lid at the tropopause (TRAP hereafter), (ii) a radiating regime with a high model lid and constant N (RAD1 hereafter), (iii) a radiating regime with a high model lid but different values of N in the troposphere and stratosphere (RAD2 hereafter). For cases (ii) and (iii) we follow §2.6 and take the model lid at $H = 64H_t = 640$ km. We choose the maximum buoyancy forcing to be $S_0 = 3.6 \times 10^{-5} \text{ m s}^{-3}$, which, using equation (3), corresponds to a maximum heating rate $Q_{\max} = 0.001 \text{ K s}^{-1}$, and a maximum rainfall rate of 14 mm hr^{-1} , typical of a cumulonimbus storm. Note, our heating rate is half of that used by Nicholls et al. (1991). Note also that, since our system is linear, any other choice of S_0 will scale the solution accordingly.

3.1. Response to Steady Heating: Trapping and Radiation

In order to characterise the effects of upward radiation, we compare the response from TRAP and RAD1 (both with uniform $N = 0.01 \text{ s}^{-1}$) to steady heating with horizontal lengthscale $L = 10$ km. In TRAP, the w response takes the form shown in figure 2a, with a single non-dispersive pulse of subsidence emanating from the heating at $x = 0$, which travels uniformly at the speed c_t of the first gravity wave mode (i.e. $c_t = NH_t/\pi \approx 30 \text{ m s}^{-1}$ in the Boussinesq limit). The response is more complex in RAD1, as illustrated in figure 4, where the time evolution of both the w

and θ responses are shown. (Note that, as in §2.6, the solutions are symmetric about $x = 0$, and are only shown for $x > 0$). In the deep atmosphere, an entire spectrum of deeper gravity wave modes is excited, which travel at a range of horizontal speeds, each of which exceeds c_t . So, (i) the adjustment is communicated more rapidly into the neighbourhood of the forcing relative to TRAP, (ii) the dominant tropospheric response now inevitably disperses, leading to a reduction in the magnitude of the tropospheric response in w relative to TRAP.

This reduction is quantified in figure 5, which shows the maximum tropospheric value of $|w|$ for $|x| > 100$ km. This automatically excludes the steady w response around $x = 0$, and instead focusses on the outwardly propagating subsidence pulse. For TRAP, $|w|_{\max} \approx 0$ until $t \approx 50$ mins (i.e., $t \approx 100$ km/ c_t , when the single gravity wave appears), after which it rises and then quickly settles to a constant value, since this pulse is non-dispersive. For RAD1, there is a signature in $|w|_{\max}$ for smaller times (due to the spectrum of deeper and faster gravity wave modes), and then decay at large times. For these parameters, the implied maximum in $|w|$ is only 20% of that in TRAP: the remote response with upward radiation is significantly less than with a lid. We return to this issue in § 3.3, where the case RAD2 is discussed.

3.2. Steady versus Transient Heating

We now consider differences between the response for steady heating (applied for all $t > 0$), and pulsed heating (applied only for $0 < t < T$, as in equation (13)). Figure 6 shows the response in w and θ at $t = 60$ mins, for each of TRAP, RAD1 and RAD2 with $T = 30$ mins. In all cases, the remote tropospheric response consists of a pulse of negative w , followed by an elongated pulse of positive θ , then a pulse of positive w , after which the response dies out.

Figure 7 provides a more detailed comparison between steady heating and a (different) case with $T = 60$ min. Shown is the time-evolution of the horizontal variation of the vertically-averaged tropospheric w (broken) and θ (solid) responses. Since heating is steady for the initial 60 mins in both cases, the responses are identical, as shown in panels (a) and (b). Panels (c) and (d) show results from a simulation where heating is steady for all time, whilst (e) and (f) show results from a simulation where heating

is terminated at 60 mins. In the pulsed case, note the regions of ascent, which propagate away from $x = 0$ immediately after heating terminates. The maximum values of w decrease with time, in exactly the same way as shown in figure 5 for the preceding subsidence pulse. However, the regions of vertically-averaged ascent give values of w that remain significant for the initiation of convection (in the sense to be discussed in §3.4) for up to 4 hrs after initiation of heating.

3.3. Effects of a Model Stratosphere

Whilst interrogation of RAD1 has been informative on the tropospheric response, in reality N varies with height. We model this using a piecewise constant $N(z)$, with $N_t = 0.01 \text{ s}^{-1}$ in the troposphere, and $N_s = 0.02 \text{ s}^{-1}$ in the stratosphere (RAD2). Since the jump in N at the tropopause leads to partial reflection of upwardly propagating waves (e.g. Sutherland 1996), RAD2 is expected to be an intermediate case between TRAP (total wave reflection at rigid lid) and RAD1 (no tropopause, so no wave reflection). Note that in RAD2 the choice $N_s = 2N_t$, $N_t = 0.01 \text{ s}^{-1}$ is physically representative.

Figure 6(c,d) shows the response after 60 mins in RAD2 to a pulsed heating of length 30 mins. The response in RAD2 has the same general form as that in RAD1, although in RAD2 the dominant tropospheric response propagates slightly faster (consistent with the larger average values of N in RAD2), and is more intense (consistent with the anticipated wave reflection at the tropopause). Of course, the tropospheric response in TRAP is stronger still. This is confirmed in figure 8 which shows the horizontal variation of the vertically-averaged tropospheric responses shown in figure 6. The peak values of $|w|$ in RAD1 and RAD2 are 50% and 30% of those in TRAP, whilst the peak values of $|\theta|$ are 70% and 60% of those in TRAP. Apparent is the increased dispersion of the dominant response in RAD1 and RAD2 (as higher order modes of varying speed contribute to the adjustment), although the timing of the peak responses remains constant across all configurations. The time evolutions of the corresponding first subsidence pulses are shown in figure 5, for the simpler case of steady heating (i.e. where there is no trailing pulse of ascent). Note how the (remote) response in RAD2 is consistently 50-100% higher than in RAD1 over $1 \text{ h} < t < 4 \text{ h}$.

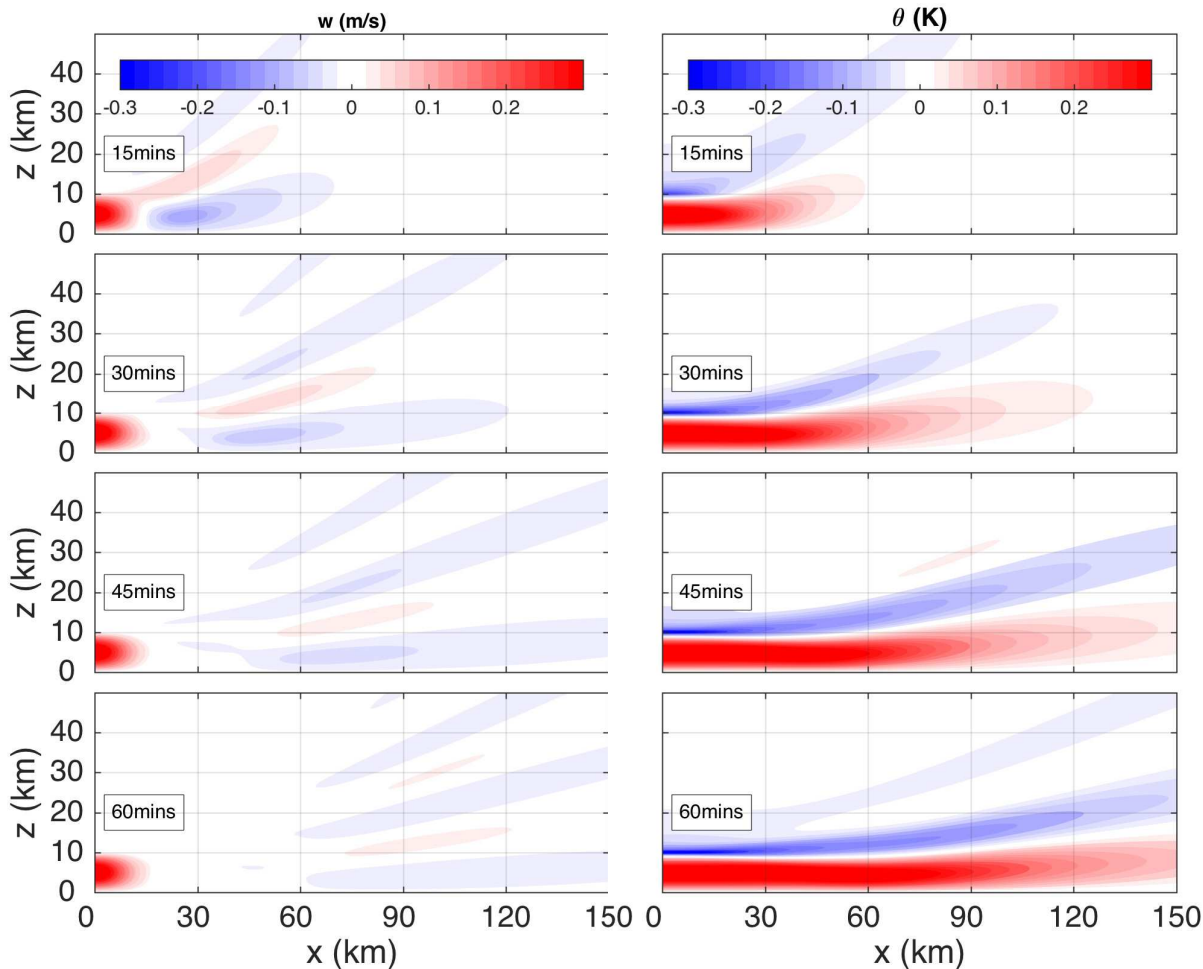


Figure 4. The time evolution of the response for w (left) and θ (right) to steady heating with $L = 10$ km, uniform $N = 0.01 \text{ s}^{-1}$, $H = 640$ km in RAD1. Note that t increases down each column.

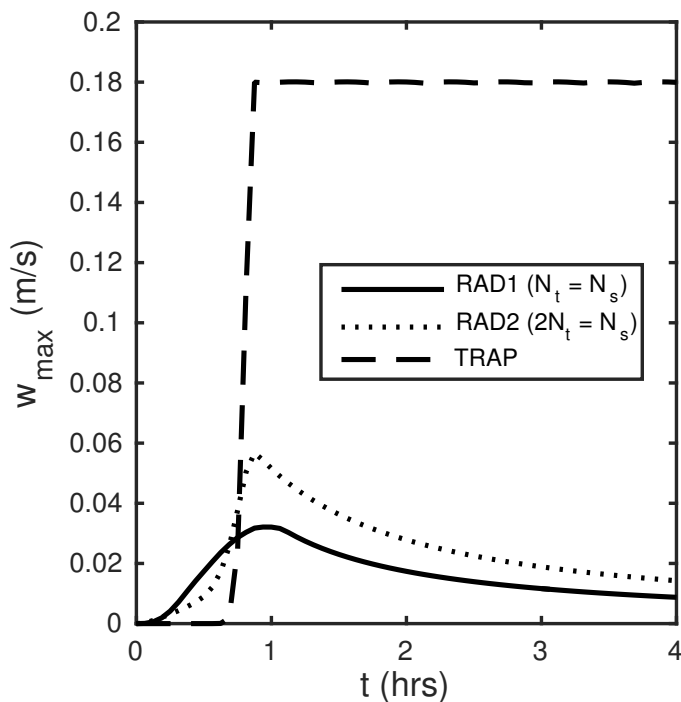


Figure 5. Time series of maximum tropospheric values of $|w|$ for $|x| > 100$ km when forced with a steady heating of width $L = 10$ km.

Although the above choice $N_s = 2N_t$ for RAD2 is physically realistic, it is interesting to examine how the response depends

upon the ratio N_s/N_t (with $N_s/N_t = 1$ corresponding to RAD1). For a 60 min pulse of heating, with $L = 10$ km, $N_t = 0.01 \text{ s}^{-1}$ and a range of values of N_s , we have computed the upward energy flux, pw , at the tropopause $z = H_t$ at a fixed time of $t = 60$ mins. We denote the horizontal average of pw over 100 km by q_z . This is shown in figure 9. As expected, the upwards radiation is maximised when $N_s = N_t$, i.e., when there is no wave reflection at the tropopause, consistent with the results of Sutherland (1996; 2010), who considered the simple case of Boussinesq monochromatic waves in an unbounded atmosphere. When $N_s \neq N_t$, figure 9 shows that the upwards radiation (in energy) is reduced by up to 12% over $0.5 < N_s/N_t < 2$. This reduction is consistent with the results shown in figure 6.

3.4. Triggering of Convection

The triggering of convection is controlled by boundary-layer thermals having enough kinetic energy to overcome convective inhibition (CIN) at the top of the boundary layer (e.g. Mapes

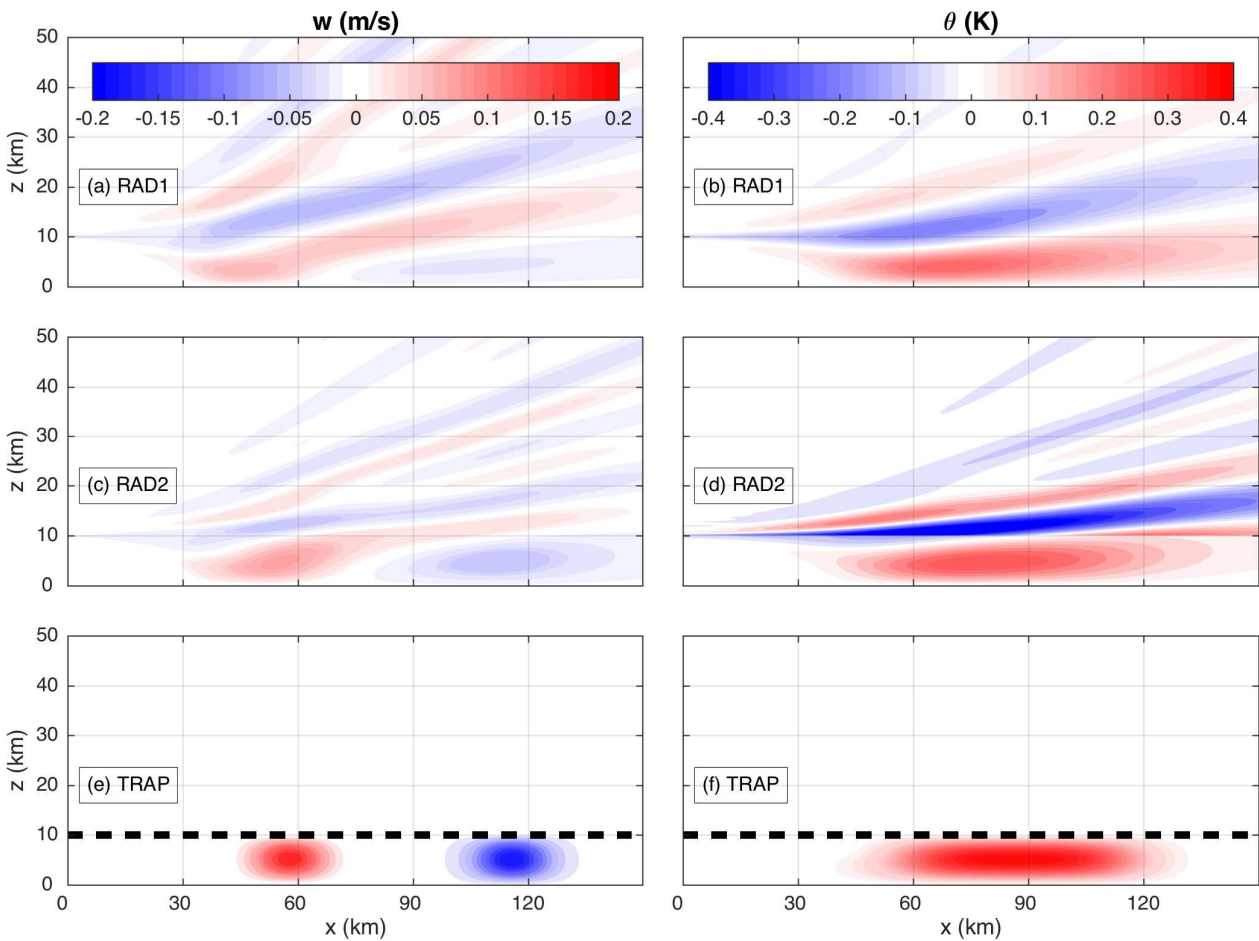


Figure 6. Response at $t = 60$ mins to a pulsed heating of length $T = 30$ mins, with $L = 10$ km, $N_t = 0.01 \text{ s}^{-1}$, $N_s = 0.02 \text{ s}^{-1}$ (RAD2 only), and $H = 640$ km (RAD1, RAD2).

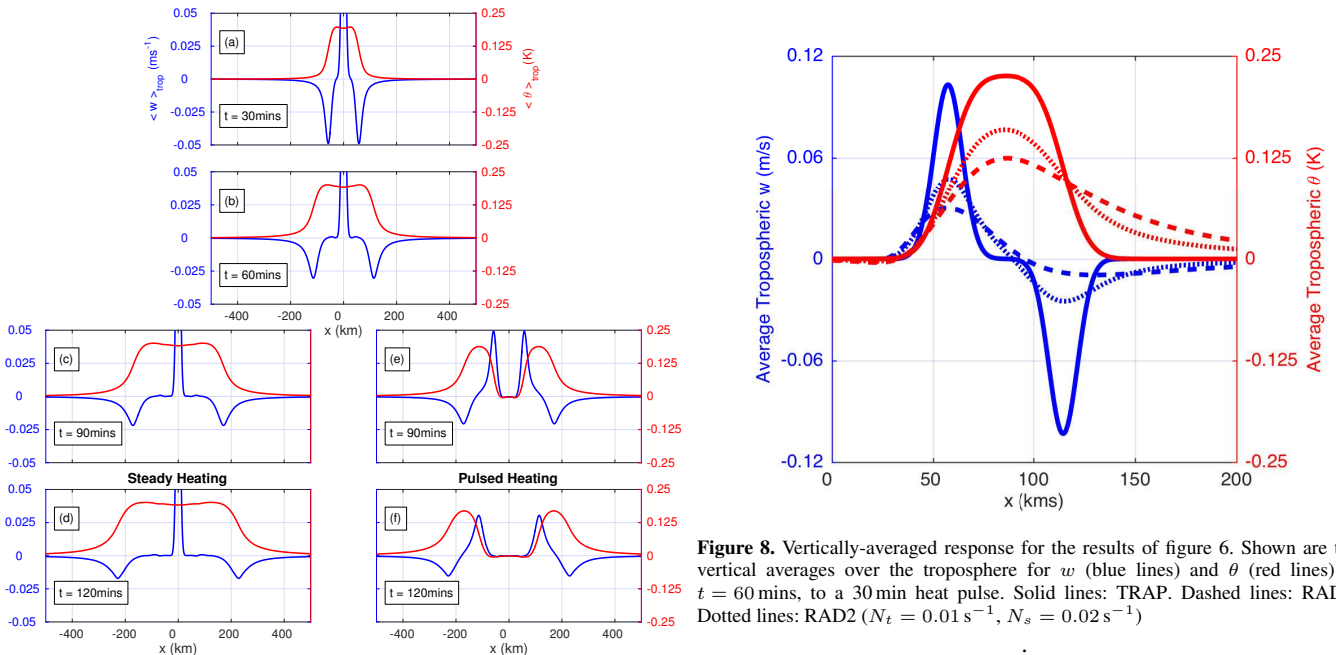


Figure 7. Vertically averaged response for steady heating (left) and a 60 min pulse of heating (right), in RAD1. Shown are vertical averages over the troposphere for w (blue lines) and θ (red lines), with $L = 10$ km, uniform $N = 0.01 \text{ s}^{-1}$, and $H = 640$ km. Panels (a,b) show the response to heating over $0 < t < T = 60$ mins (same for both steady and pulsed heating). Panels (c, d) show the response for a further 60 mins of (steady) heating. Panels (e, f) show the response when the heating is terminated after 60 mins (pulsed heating).

Figure 8. Vertically-averaged response for the results of figure 6. Shown are the vertical averages over the troposphere for w (blue lines) and θ (red lines) at $t = 60$ mins, to a 30 min heat pulse. Solid lines: TRAP. Dashed lines: RAD1. Dotted lines: RAD2 ($N_t = 0.01 \text{ s}^{-1}$, $N_s = 0.02 \text{ s}^{-1}$)

2000), and one process that can erode the CIN is low-level ascent. This acts to raise the height of any inversion at the top of the boundary layer, and can also induce convergence that enhances low-level moisture (Mapes 1993). Meanwhile, upper

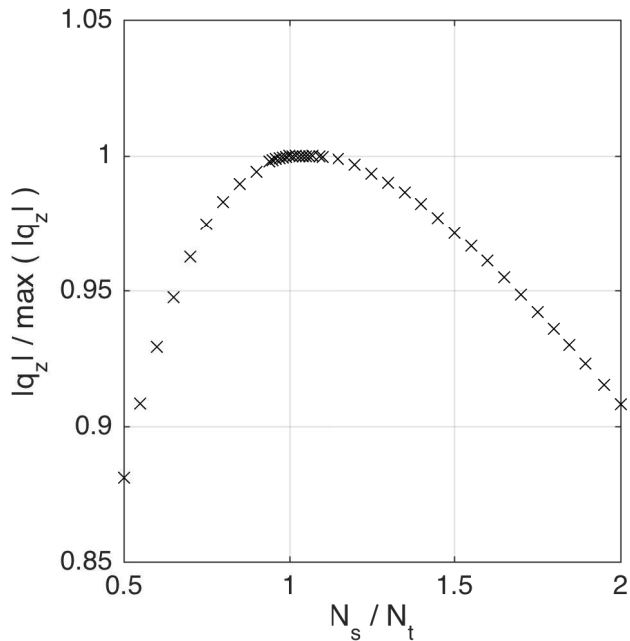


Figure 9. Horizontally-averaged vertical energy flux $|q_z| = |pw|$, at a fixed time $t = 60$ min, plotted as a function of ratio N_s/N_t , measured with our model RAD2 in response to a 60 min pulse of heating with $L = 10$ km, $N_t = 0.01 \text{ s}^{-1}$. The horizontal averaging is done over $0 < x < 100$ km. Values have been normalised by the maximum value of q_z across all values of N_s/N_t .

level subsidence acts to stabilise the troposphere, reducing the amount of CAPE.

After a localised convection event of the type modelled here by the prescribed heating, radiating gravity waves provide the necessary local dynamical adjustment (Bretherton and Smolarkiewicz 1989), which involves periods of both tropospheric descent and ascent (figure 6). The initial subsidence pulse with deep tropospheric warming provides an ambient atmosphere with reduced CAPE (i.e., less favourable for further convection), but this disappears in the following pulse, which also has low-level ascent (to erode CIN, and is thus favourable for further convection). Case studies have shown these processes to be influential in controlling the triggering of further convection close to a parent storm (e.g., Marsham and Parker 2006, Birch et al. 2013), even when w is only of the order of centimetres per second, and is thus too small to act as a direct trigger for convection.

We now use our model to identify zones where the radiating gravity waves provide an ambient atmosphere favourable for triggering of convection, in the above sense. Figure 10 shows results from RAD2 following a 1 h pulse of heating. We consider θ in the middle troposphere (shown as coloured contours) as a measure of reduced CAPE, and positive w at 1 km as a measure of CIN erosion (shown as shaded regions). Immediately after the

termination of heating at 1 h, a series of zones appear with small or negative mid-tropospheric θ and positive low-level w , each of which moves away from the parent storm and is favourable for further convection. The first such zone is highlighted within the dashed contour; this moves outwards from the parent storm at approximately 20 m s^{-1} .

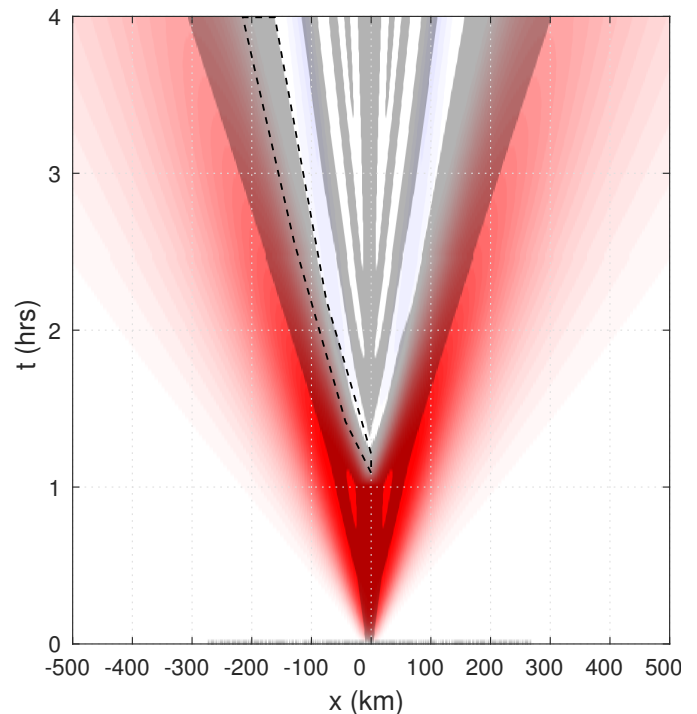


Figure 10. Hovmöller plot showing the response to a 1 hr pulse of heating in RAD2, with $L = 10$ km, $N_t = 0.01 \text{ s}^{-1}$, $N_s = 0.02 \text{ s}^{-1}$. The coloured contours show mid-tropospheric θ ; red regions, in which the atmosphere is warmed, will have reduced CAPE. The shaded region show where $w > 0$ at 1 km, which will act to erode CIN. The dashed contour encloses one of several bands that may thus be preferential for triggering of subsequent storms.

4. Implications for Convection Parameterisation Schemes and GCMs

In §3 we quantified the dynamical response to buoyancy forcing representing a single convection event with a width of about 10 km. We now investigate how the dynamical response to such an event would appear in a coarse model (e.g., a GCM) in which convection is not resolved, and is instead parametrised by applying heating over a grid cell with width of about 100 km. We consider how the local and remote responses are then altered, and the implied changes in the heating tendency.

Note that we are not considering the alternative scenario in which a population of sub-grid clouds (each of width 10 km, say) is spread over a grid cell of width 100 km (say). In that case, the differences between the exact dynamical response (excited

by a population of small-scale heatings) and that due to a single smeared-out heating (perhaps corresponding to a convection scheme) might be smaller. Our experiment, involving a single isolated sub-grid cloud, might be regarded as a “worst case scenario” for a convection scheme.

4.1. Sensitivity of Gravity Wave Response to Horizontal Length Scale of Heating

Under conditions of identical total (x -integrated) heat input, our model shows that variation in the horizontal length scale of the heating, L , induces significant changes in the timing and magnitude of the immediate and remote atmospheric adjustment. We now quantify these differences for the response to pulsed heating of duration 1 h, between cases with $L = 10$ km, and $L = 100$ km. The former is representative of single, isolated convective hot towers, whilst the latter is representative of parameterised convection in a GCM, where small length scales cannot be resolved and the heating must be imposed at the grid scale (or larger). To ensure the same total heat input in both cases, the maximum buoyancy forcing, S_0 satisfies $S_0(L = 10 \text{ km}) = 10 S_0(L = 100 \text{ km})$.

Figure 11 shows the responses in w and θ . The response is averaged both vertically over the troposphere $0 \leq z \leq 10$ km, and horizontally over $|x - x_0| \leq 50$ km for each of $x_0 = 0$ (panel a: local response directly over heating) and $x_0 = 100$ km (panel b: remote response). The horizontal averaging means we are comparing the response to “real” convection ($L = 10$ km) when smeared over a GCM grid cell of width 100 km, with the response to parameterised convection ($L = 100$ km) over the same grid cell. That is, we compare how the response *should* appear on the model grid, with how it *will* appear when convection is parameterised (ignoring any additional degradation due to the numerical scheme of the GCM, since the response here is calculated exactly via (16) and (17)).

We first discuss the local response shown in figure 11(a). When $L = 10$ km, the w response quickly reaches a steady-state value, but this “correct” value is never attained when $L = 100$ km, with w remaining smaller. It is a similar story for the θ response, but θ does eventually reach the “correct” steady-state value. When the heating is terminated at 1 hr, both w and θ decay in about 30 mins

when $L = 10$ km; but the decay takes twice as long (circa 1 h) when $L = 100$ km.

The remote response is shown in figure 11(b). Here the magnitude of the response is smaller when $L = 100$ km than when $L = 10$ km, for both w and θ . There is also a non-trivial change in the timing of the peak warming, which occurs too soon (by about 15 mins) when $L = 100$ km. However, the eventual decay (for $t > 2$ h) is similar in both cases.

There are implications for the accuracy of the entire dynamical adjustment in GCMs when small-scale convective heating ($L = 10$ km) is replaced by smeared-out parametrised heating on the grid scale ($L = 100$ km). In particular, this induces errors of about 20% in magnitude in both w and θ , for both the local and remote responses. Any dynamical processes sensitive to w and θ will be correspondingly compromised. For example, the suppression and initiation of further convection will be modified, via the CAPE and CIN mechanisms discussed in §3.4. We stress that such modifications are possible even though the absolute differences in w are only $1 - 2 \text{ cm s}^{-1}$: these differences would be insignificant for direct triggering of convection, but they will imply 20% differences in quantities such as CAPE and CIN.

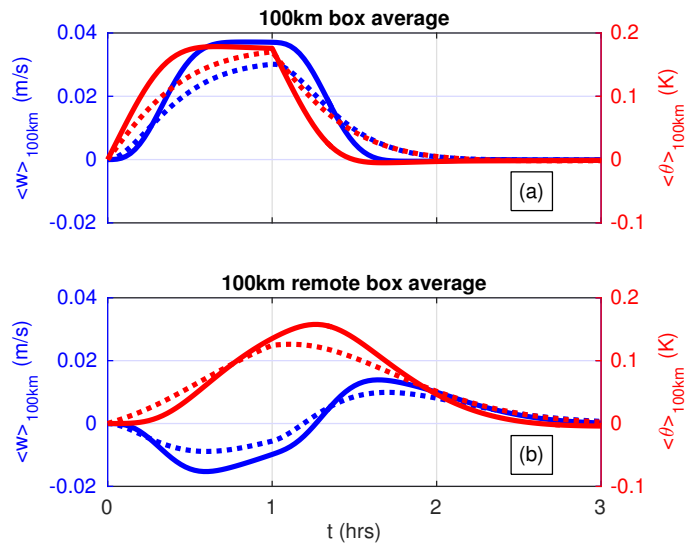


Figure 11. Time evolution of the averaged tropospheric responses in RAD2 when $L = 10$ km (solid lines) and $L = 100$ km (dotted lines). Shown are w (blue) and θ (red), with additional horizontal averaging over (a) $-50 \text{ km} < x < 50 \text{ km}$ (local response) and (b) $50 \text{ km} < x < 150 \text{ km}$ (remote response).

Looking at figure 11, one might conclude that, despite differences in the first few hours after initiation, both cases of heating are in some agreement by around 3 hours. However, figure 12, which is an instantaneous vertical cross section of the corresponding fields at $t = 4$ hours, reveals anomalies in

the vertical structure. Here, $\Delta w \equiv (w(L = 100 \text{ km}) - w(L = 10 \text{ km}))$ and $\Delta\theta \equiv (\theta(L = 100 \text{ km}) - \theta(L = 10 \text{ km}))$.

In summary, from figures 11 and 12 we conclude that narrow, intense heating, representing a convective hot tower, induces the largest velocities and warming. Less intuitive is the observation that the differences in behaviour persist for several hours. Coarse GCM models with parameterised heating will fail to resolve some of the variation in responses and, hence, fail to simulate modification of the convective environment.

Note that the results of this section can also be interpreted in a completely different way, in which we are comparing the dynamical responses induced by two fundamentally different kinds of convection. Then, the narrow intense heating ($L = 10 \text{ km}$) models a single isolated hot tower, whilst the wider less intense heating ($L = 100 \text{ km}$) models a mesoscale convective system.

4.2. Redistribution of heating

GCM parameterisation schemes generally make the assumption that all subsidence happens within the convecting grid box (Arakawa and Schubert 1974). In this section we estimate the error associated with the spatial homogenisation (or smoothing-out) of the grid-box heating (implicit in a GCM) by comparing adjustments with more realistic heating distributions. Once again, we will consider the “worst case scenario” where convective heating in the grid box is confined to a single hot tower.

An appreciation of the error associated with GCM-like smoothing of heating can be achieved through analysis of the heating tendency field, $\frac{\partial b}{\partial t}$. From (1) recall:

$$\frac{\partial b}{\partial t} = S - N^2(z)w. \quad (37)$$

For steady heating (which allows a constant value of b to develop at all positions in the domain), in the long-time limit, a steady-state $\frac{\partial b}{\partial t} = 0$ develops, when there is a balance between heating and w response fields, with $S(x, z, t) - N^2(z)w(x, z, t) = 0$.

To consider the dynamics of tendency in the context of GCMs, it is first necessary to ensure that all heating is contained within the spatial domain of our model. For the purposes of this section (alone) we therefore re-define the x -dependence in our buoyancy

forcing function, $S(x, z, t)$, to be a simple box function

$$X(x) = \Theta\left(x + \frac{L}{2}\right) - \Theta\left(x - \frac{L}{2}\right), \quad (38)$$

where, recall Θ is the Heaviside function. Whilst the Gaussian x -dependence used elsewhere in this study is more realistic, a box function has no tail, and therefore all heating is contained within the domain which, for present purposes, we regard equivalent to a parent grid box. We shall consider two cases. The horizontal heating variation, $X(x)$, is taken to have i) a realistic horizontal scale with $L = 10 \text{ km}$, representative of a single cloud, and ii) a GCM-like smoothed scale with $L = 100 \text{ km}$. In both cases, the total heating is ensured to be the same by setting $S_0(L = 10 \text{ km}) = 10S_0(L = 100 \text{ km})$. This choice of $X(x)$ may be straightforwardly implemented in (16) for w , and then in (20) for b , with G taken as

$$\begin{aligned} G(c_j, L, x, t) &= \Theta(ct - x + L)(ct - x + L)/L \quad (39) \\ &- \Theta(ct - x - L)(ct - x - L)/L \\ &- \Theta(-ct - x + L)(-ct - x + L)/L \\ &+ \Theta(-ct - x - L)(-ct - x - L)/L. \end{aligned}$$

Figure 13 compares the instantaneous spatial integral (in x and z) of tropospheric heating tendency over a 100 km box (centred on $x = 0$) for our chosen cases (i) and (ii) above. The differences between the red and blue lines represents the error introduced when there is smoothing of heating. Shown also is the heating tendency time series of a scaled heating (black line), which we shall discuss later in this section.

In the $L = 10 \text{ km}$ heating case, the propagating modes of subsidence take time to propagate outside the 100 km box. Thus for a small time almost all the subsidence is within the box, and the average tendency, $\langle \partial b / \partial t \rangle$, is almost constant. As the descending modes move through the edges of the 100 km box, subsidence transfers to neighbouring regions and the tendency within the box falls. In contrast, when the heating is artificially smoothed over the 100 km box (red line), the subsidence immediately occurs outside the box and tendency is immediately reduced inside the parent box, as the vertical motion begins to compensate the heating term. However, at around 25 mins, the

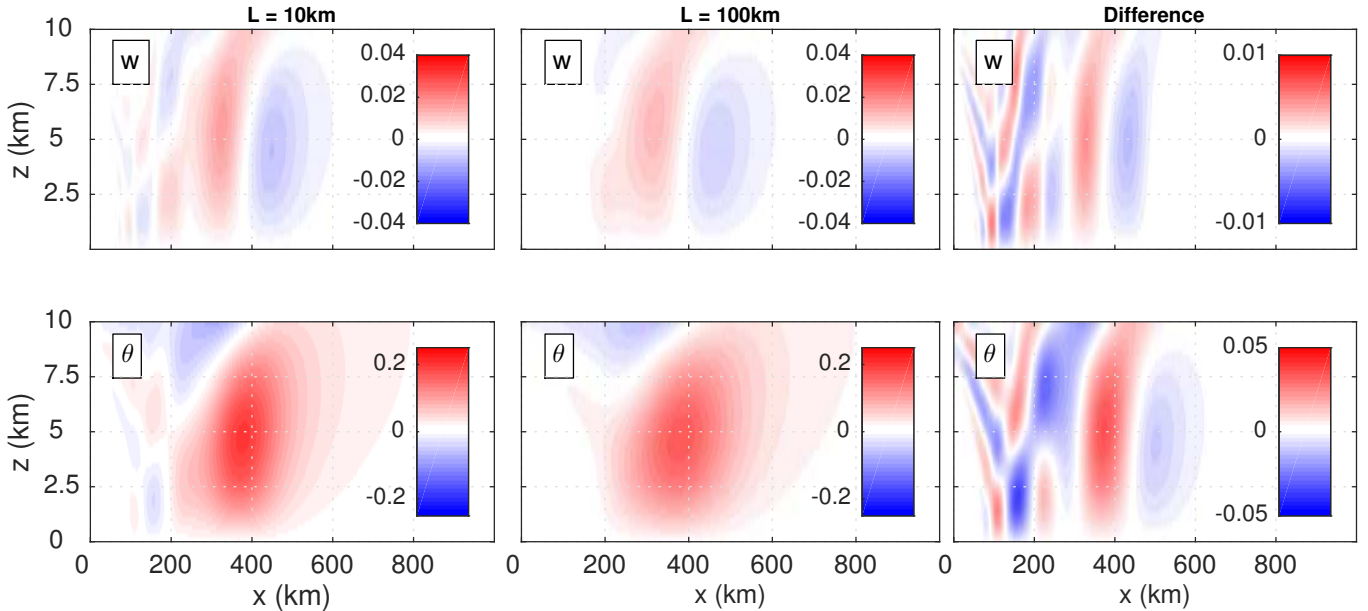


Figure 12. Vertical cross sections of w (ms^{-1}) and θ (K) response to forcing of horizontal lengths $L = 10$ km (top) and $L = 100$ km (bottom), which is pulsed for $t = 1$ hr. The response at $t = 4$ hrs is shown. The right hand column is the difference. Total heating is the same in both cases.

blue line sinks below the red, and it approaches equilibrium faster than its smooth counterpart thereafter. This behaviour is consistent with the longer tendency modes in the smoothed heating taking more time to separate-out and to leave the parent box.

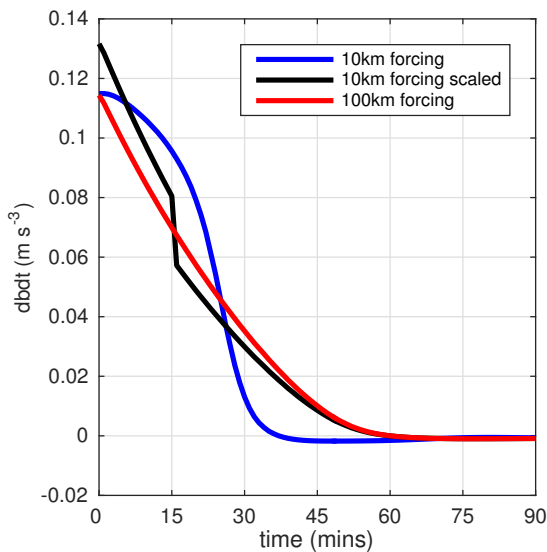


Figure 13. Time series of 100km spatially integrated heating tendencies for a 10 km realistic heating (blue), a 100 km smoothed GCM-like heating (red) and a scaled 100 km heating (black). Total heating is the same in both cases. The difference between the red and blue lines represents a time-local error in heating tendency which arises as a consequence of spatial smoothing of heating, over the domain (GCM box). The black line shows a scaled heating (see text) which has a reduced error in the parent grid box.

A further comparison is made in figure 14, which shows Hovmöller plots of the difference between tropospheric heating tendency for the cases (i) and (ii) described above. Shown is a high-resolution solution, in which heating is considered to be structured within the GCM box, and the same solution coarsened to GCM-like resolution ($\Delta x = 100$ km, $\Delta t = 15$ mins) via spatial

and temporal box averaging. Again we observe subsidence modes warming neighbouring grid boxes immediately in the smooth case, and the heating tendency persisting in the parent grid box for longer. The parent grid box is therefore too cold for the first 30 mins and too warm for the subsequent 30 mins, with errors of the order of 10% apparent. The adjacent grid boxes mirror these differences for the first hour. Differences in the following hour are attributed to the longer modes generated from the smooth heating dispersing the envelope of dominant response (the narrow heating has a tighter envelope). Differences in the parent and adjacent grid box after 2 hours are minimal (this fact is also visible in figure 13). The domain far-field response shows minimal difference throughout the simulation.

The errors apparent in figures 13 and 14 suggest a calibration might fruitfully be applied to GCM heating parameterisation schemes, to compensate for the thermodynamic errors associated with incorrect propagation of the subsidence response away from heating. We postulate a simple multiplicative scaling to the smoothed GCM-like heating, designed to produce a response closer to that observed in a calculation forced with a more realistic (i.e. narrow) horizontal variation of heating. Put another way, we propose to scale the time-dependence of the forcing in such a way that the red line in figure 13 moves closer to the blue line. Accordingly, comparing the smoothed heating with the narrow, it is apparent that the smoothed heating requires an increased

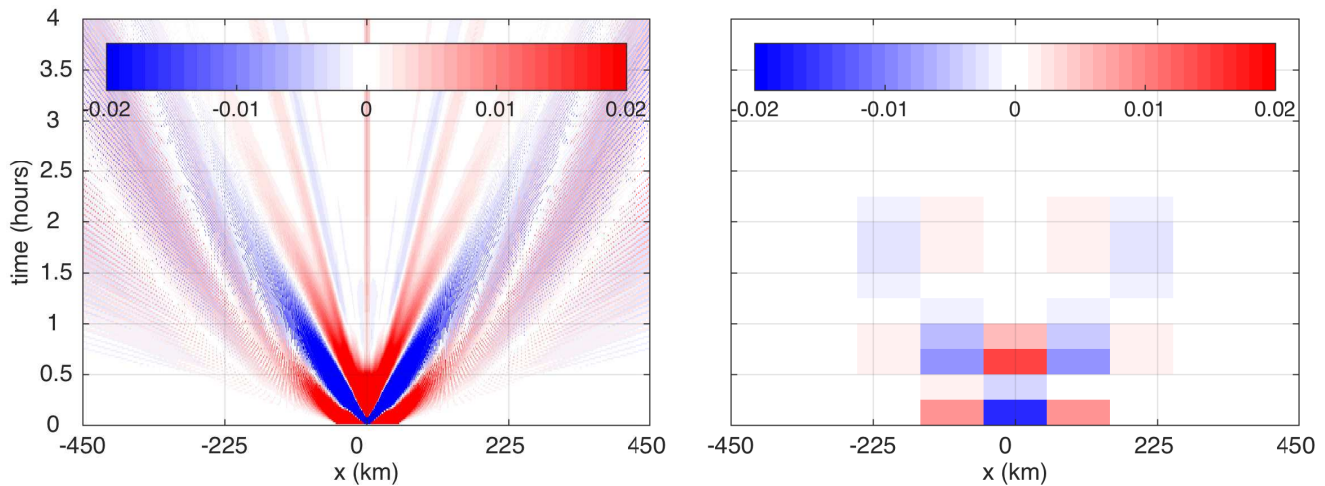


Figure 14. Hovmöller plot of differences in tropospheric heating tendency (m s^{-3}) between the non-scaled cases considered in figure 13. Panel (a) shows a fully resolved solution, panel (b) shows a solution which has been coarsened to 100 km grid box and 15 min time step (representative of a GCM). In the parent grid box, the smoothed heating is too cold at 30 mins, then too warm for 30 mins, before reconciling with the realistic case.

amplitude for some time, followed by a decreased amplitude, before returning back to its original amplitude for later times, when the responses to smooth and narrow forcing have reconciled. Denote the first time at which the lines in figure 13 cross by T_1 and that at which both reach equilibrium by T_2 . For $0 < t < T_1$, we scale the heat-forcing by factor $\alpha_1 > 1$, for $T_1 < t < T_2$ we scale it by $\alpha_2 < 1$, and for $t > T_2$ no scaling is applied i.e. we return the buoyancy forcing to its nominal value.

We now seek to minimise the area between the red and blue curves of figure 13. We apply the following practical constraints:

1. T_1, T_2 are chosen to be multiples of 15 minute blocks.

From inspection of figures (13) and (14), we choose $T_1 = 30$ mins, $T_2 = 60$ mins.

2. $(\alpha_1 - 1)T_1 = (1 - \alpha_2)T_2 \implies \alpha_2 = \frac{T_1 + T_2 - \alpha_1 T_1}{T_2}$.

Constraint 2 is chosen to ensure that total heat input is the same in both the scaled and non-scaled cases for $t > T_2$.

Using an overall cost parameter, ξ , defined as

$$\xi = \left\langle \left\langle \left\langle \frac{\partial b^{(1)}}{\partial t} \right\rangle_{x,z} - \left\langle \frac{\partial b^{(2)}}{\partial t} \right\rangle_{x,z} \right\rangle_t \right\rangle, \quad (40)$$

where $b^{(1)}$ is the buoyancy response to a $L = 10$ km forcing and $b^{(2)}$ is the buoyancy response to a $L = 100$ km forcing, and the averaging is done over the troposphere in the central 100 km box. We measure the error, and minimise it over $1 < \alpha_2 < 1.5$. We find an initial forcing amplification of $\alpha_1 = 1.15$ and then a forcing suppression of $\alpha_2 = 0.85$. The black line in figure 13

shows data from our time-variant scaled smooth heating, which is now closer to the blue in the parent grid box. However, whilst our scaling *ansatz* may improve the response in the parent grid box, the response in the adjacent field shows the expected increase in error, as shown in figure 15.

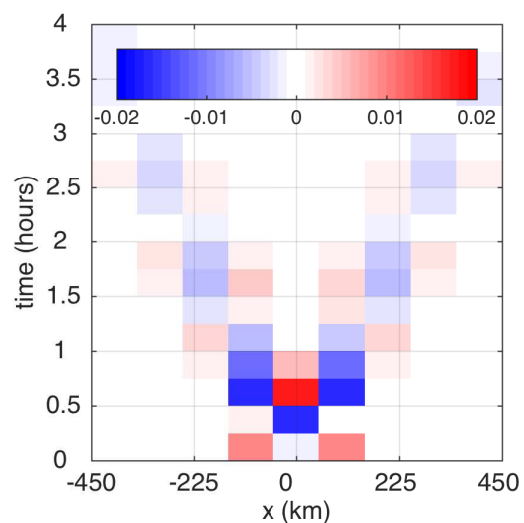


Figure 15. Hovmöller plot of differences in buoyancy tendency (m s^{-3}) between a 10km forcing and a 100km forcing which has been scaled in order to reduce error (see text). The parent box now has a reduced error to begin, but the far field has an increased error.

In this section, we have quantified error associated with the smoothing-out of convective heating in a manner similar to that performed in GCM-models. We have proposed a mechanism to improve the grid-box response, with a simple time-dependent heating parameterisation. Whilst this parameterisation led to error reduction in the parent grid box, the adjacent and neighbouring grid boxes experience increased error. Whether it is possible

to improve the parameterisation, with more sophisticated time-dependent heating remains an open question not addressed here. Certainly, one place to start would be with a more rigorous analysis of the parameter space influencing the error, together with consideration of a global error.

5. Conclusion

Using an analytical solution to a 2D thermally-forced, deep atmosphere, we have constructed an idealised model of convective adjustment. We have expressed vertical velocity and potential temperature response in terms of convectively-forced gravity wave modes and, hence, we have illuminated the role of these modes in conditioning the troposphere for further convection. We find that the characteristics of our forced gravity waves are influenced by the spatial and temporal dependence of the forcing function, the nature of the upper boundary condition applied to the domain, and upon model stratification.

We tested the influence of the upper boundary condition and found that a trapped solution with rigid lid at the tropopause (allowing no wave radiation into the stratosphere), yields a single gravity mode, communicating high intensity downward motion and warming, which propagates into the neighbouring troposphere and inhibits the chance of further convection. Raising the altitude of the upper lid high into the mesosphere and beyond (to approximate the semi-infinite solution) allows a range of higher-order gravity wave modes to be excited, with much deeper and faster modes acquiring importance. The convective adjustment is therefore communicated into the immediate environment faster than in the trapped case. We note also that allowing waves to radiate upward sees a reduction in the magnitude and intensity of the tropospheric response, as expected.

Investigating the temporal dependence of gravity wave characteristics through a pulsed forcing function, we find that when the pulse of forcing is truncated, a rebound mode of upward motion propagates away from the initially heated region, and the potential temperature response returns to base state. Further, using figure 10, we identify propagating zones where the radiating gravity waves provide an ambient atmosphere favourable for further convection. In such zones, there is no longer tropospheric

subsidence (which reduces CAPE), and there is low-level ascent which will erode CIN.

The inclusion of a model stratosphere, with $N_s = 2N_t$ increases the intensity of the tropospheric response, due to wave reflection at the tropopause. We also notice a slight increase in the propagation speed of the mode of dominant response. We find a maximum of energy radiated into the stratosphere (communicated by gravity waves) for $N_t = N_s$, as there is no interface and therefore no reflection. With this in mind, we consider our trapped model (TRAP) and optimally-radiating model (RAD1) as respective lower and upper bounds on radiation at the tropopause. The most realistic intermediate model (RAD2, with $N_t = 2N_s$), which has partial trapping and radiation, has upward radiation between the two bounds.

We quantify the error associated with smoothing out convective heating from a subgrid, single convective hot tower onto a coarse GCM grid. Performing “worst case scenario” experiments, in which a convection scheme spreads heating from a cloud of width 10 km over a full model grid box of width 100 km, we find that the timing and magnitude of the adjustment is dependent on the heating distribution. Perturbations in potential temperature and vertical velocity will be distributed faster and over a larger region in the parameterised case. Furthermore, an isolated cloud has a strong response on a sub-GCM-grid scale, which has implications for the forcing of neighbouring grid cells in current numerical models, since the timing and magnitude of the response, communicated by gravity waves, is sensitive to the horizontal length scale of the forcing function. Further, analysis of the heating tendency reveals errors of the order of 20% and correspond to a grid-box heating tendency which falls too quickly when heating is spatially smoothed (parameterised), due to a failure to account for the finite time taken by small-scale responses to propagate out of the grid-box. We propose a simple time-varying scaling to the heating to minimise these errors. Such a scaling decreases the error in the grid box that is the parent to convection, but increases error in adjacent boxes. We propose ways in which to potentially improve this scaling, but leave this for another study.

The analytical model developed in this work allows us to draw conclusions on the role of convectively forced gravity

waves. Notably, even with maximum upward energy radiation, we observe a significant tropospheric response to prescribed thermal forcing. Further, the gravity wave characteristics associated with the convective adjustment are highly sensitive to the upper boundary condition at the tropopause, heating function and model stratosphere.

Acknowledgements

We thank the Leeds/York NERC Doctoral Training Programme and UK Met Office for providing funding for Oliver Halliday (NE/L002574/1). Griffiths and Parker are supported by the GENESIS project (NE/N013840/1) as part of the joint NERC / Met Office ParaCon programme. Parker is also supported by a Royal Society Wolfson Research Merit Award (2014–2018).

References

- Andersen, J. A. and Kuang, Z. (2008). A toy model of the instability in the equatorially trapped convectively coupled waves on the equatorial beta plane. *J. Atmos. Sci.*, 65(12):3736–3757.
- Arakawa, A. and Schubert, W. H. (1974). Interaction of a cumulus cloud ensemble with the large-scale environment, part i. *J. Atmos. Sci.*, 31(3):674–701.
- Arfken, G. B. (2013). *Mathematical methods for physicists*. Academic press.
- Barnes, G. and Sieckman, K. (1984). The environment of fast-and slow-moving tropical mesoscale convective cloud lines. *Monthly Weather Review*, 112(9):1782–1794.
- Birch, C., Parker, D., O’Leary, A., Marsham, J., Taylor, C., Harris, P., and Lister, G. (2013). Impact of soil moisture and convectively generated waves on the initiation of a West African mesoscale convective system. *Quart. J. Roy. Meteor. Soc.*, 139(676):1712–1730.
- Bretherton, C. S. and Smolarkiewicz, P. K. (1989). Gravity waves, compensating subsidence and detrainment around cumulus clouds. *J. Atmos. Sci.*, 46(6):740–759.
- Bushell, A. C., Butchart, N., Derbyshire, S. H., Jackson, D. R., Shutts, G. J., Vosper, S. B., and Webster, S. (2015). Parameterized gravity wave momentum fluxes from sources related to convection and large-scale precipitation processes in a global atmosphere model. *J. Atmos. Sci.*, 72(11):4349–4371.
- Chumakova, L. G., Rosales, R. R., and Tabak, E. G. (2013). Leaky rigid lid: New dissipative modes in the troposphere. *J. Atmos. Sci.*, 70(10):3119–3127.
- Edman, J. P. and Romps, D. M. (2017). Beyond the rigid lid: Baroclinic modes in a structured atmosphere. *J. Atmos. Sci.*, 74(11):3551–3566.
- Emanuel, K. A. (1986). An air-sea interaction theory for tropical cyclones. Part I: Steady-state maintenance. *J. Atmos. Sci.*, 43(6):585–605.
- Emanuel, K. A., David Neelin, J., and Bretherton, C. S. (1994). On large-scale circulations in convecting atmospheres. *Quart. J. Roy. Meteor. Soc.*, 120(519):1111–1143.
- Fovell, R., Durran, D., and Holton, J. (1992). Numerical simulations of convectively generated stratospheric gravity waves. *J. Atmos. Sci.*, 49(16):1427–1442.
- Gill, A. E. (1982). *Atmosphere-ocean dynamics*. Elsevier.
- Gregory, D. and Rowntree, P. (1990). A mass flux convection scheme with representation of cloud ensemble characteristics and stability-dependent closure. *Monthly Weather Review*, 118(7):1483–1506.
- Hankinson, M. C., Reeder, M., and Lane, T. (2014). Gravity waves generated by convection during TWP-ICE: I. inertia-gravity waves. *J. Geophys. Research: Atmospheres*, 119(9):5269–5282.
- Holton, J., Beres, J., and Zhou, X. (2002). On the vertical scale of gravity waves excited by localized thermal forcing. *J. Atmos. Sci.*, 59(12):2019–2023.
- Holton, J. R. and Alexander, M. (1999). Gravity waves in the mesosphere generated by tropospheric convection. *Tellus A*, 51(1):45–58.
- Kim, S. H., Chun, H.-Y., and Jang, W. (2014). Horizontal divergence of typhoon-generated gravity waves in the upper troposphere and lower stratosphere (UTLS) and its influence on typhoon evolution. *Atmospheric Chemistry and Physics*, 14(7):3175–3182.
- Kim, S.-Y. and Chun, H.-Y. (2011). Impact of typhoon-generated gravity waves in the typhoon development. *J. Geophys. Research: Letters*, 38(1).
- Lac, C., Lafore, J., and Redelsperger, J. (2002). Role of gravity waves in triggering deep convection during TOGA COARE. *J. Atmos. Sci.*, 59(8):1293–1316.
- Lane, T. P. and Reeder, M. J. (2001). Convectively generated gravity waves and their effect on the cloud environment. *J. Atmos. Sci.*, 58(16):2427–2440.
- Lane, T. P., Reeder, M. J., and Clark, T. L. (2001). Numerical modeling of gravity wave generation by deep tropical convection. *J. Atmos. Sci.*, 58(10):1249–1274.
- Lane, T. P. and Zhang, F. (2011). Coupling between gravity waves and tropical convection at mesoscales. *J. Atmos. Sci.*, 68(11):2582–2598.
- Lindzen, R. and Tung, K. (1976). Banded convective activity and ducted gravity waves. *Monthly Weather Review*, 104(12):1602–1617.
- Lindzen, R. S. (1974). Wave-CISK in the tropics. *J. Atmos. Sci.*, 31(1):156–179.
- Liu, C. and Moncrieff, M. W. (2004). Effects of convectively generated gravity waves and rotation on the organization of convection. *J. Atmos. Sci.*, 61(17):2218–2227.
- Mapes, B. E. (1993). Gregarious tropical convection. *J. Atmos. Sci.*, 50(13):2026–2037.
- Mapes, B. E. (1998). The large-scale part of tropical mesoscale convective system circulations. *J. Meteor. Soc. of Japan Series 2*, 76(1):29–55.
- Mapes, B. E. (2000). Convective inhibition, subgrid-scale triggering energy, and stratiform instability in a toy tropical wave model. *J. Atmos. Sci.*,

- 57(10):1515–1535.
- Marsham, J. and Parker, D. (2006). Secondary initiation of multiple bands of cumulonimbus over southern Britain. II: Dynamics of secondary initiation. *Quart. J. Roy. Meteor. Soc.*, 132(617):1053–1072.
- Nicholls, M. E. (1987). A comparison of the results of a two-dimensional numerical simulation of a tropical squall line with observations. *Monthly Weather Review*, 115(12):3055–3077.
- Nicholls, M. E., Pielke, R. A., and Cotton, W. R. (1991). Thermally forced gravity waves in an atmosphere at rest. *J. Atmos. Sci.*, 48(16):1869–1884.
- Ong, H., Wu, C.-M., and Kuo, H.-C. (2017). Effects of artificial local compensation of convective mass flux in the cumulus parameterization. *J. Adv. Model. Earth Syst.*, 9:1811–1827.
- Pandya, R. E., Durran, D. R., and Weisman, M. L. (2000). The influence of convective thermal forcing on the three-dimensional circulation around squall lines. *J. Atmos. Sci.*, 57(1):29–45.
- Parker, D. J. and Burton, R. R. (2002). The two-dimensional response of a tropical jet to propagating lines of convection. *J. Atmos. Sci.*, 59(7):1263–1273.
- Piani, C., Durran, D., Alexander, M., and Holton, J. (2000). A numerical study of three-dimensional gravity waves triggered by deep tropical convection and their role in the dynamics of the QBO. *J. Atmos. Sci.*, 57(22):3689–3702.
- Raymond, D. J. (1983). Wave-CISK in mass flux form. *J. Atmos. Sci.*, 40(10):2561–2574.
- Rotunno, R., Klemp, J. B., and Weisman, M. L. (1988). A theory for strong, long-lived squall lines. *J. Atmos. Sci.*, 45(3):463–485.
- Schmidt, J. M. and Cotton, W. R. (1990). Interactions between upper and lower tropospheric gravity waves on squall line structure and maintenance. *J. Atmos. Sci.*, 47(10):1205–1222.
- Shige, S. and Satomura, T. (2000). The gravity wave response in the troposphere around deep convection. *J. Meteor. Soc. of Japan Series 2*, 78(6):789–801.
- Shutts, G. and Gray, M. (1994). A numerical modelling study of the geostrophic adjustment process following deep convection. *Quart. J. Roy. Meteor. Soc.*, 120(519):1145–1178.
- Stensrud, D. J. (2009). *Parameterization schemes: keys to understanding numerical weather prediction models*. Cambridge University Press.
- Stephens, G. L., L'Ecuyer, T., Forbes, R., Gettleman, A., Golaz, J.-C., Bodas-Salcedo, A., Suzuki, K., Gabriel, P., and Haynes, J. (2010). Dreary state of precipitation in global models. *J. Geophys. Research: Atmospheres*, 115(D24).
- Sutherland, B. (1996). Internal gravity wave radiation into weakly stratified fluid. *Physics of Fluids (1994-present)*, 8(2):430–441.
- Sutherland, B. R. (2010). *Internal gravity waves*. Cambridge University Press.
- Thorpe, A., Miller, M., and Moncrieff, M. (1982). Two-dimensional convection in non-constant shear: A model of mid-latitude squall lines. *Quart. J. Roy. Meteor. Soc.*, 108(458):739–762.
- Tulich, S. N., Kiladis, G. N., and Suzuki-Parker, A. (2011). Convectively coupled Kelvin and easterly waves in a regional climate simulation of the tropics. *Climate Dynamics*, 36(1-2):185–203.
- Tulich, S. N. and Mapes, B. E. (2008). Multiscale convective wave disturbances in the tropics: Insights from a two-dimensional cloud-resolving model. *J. Atmos. Sci.*, 65(1):140–155.
- Tulich, S. N., Randall, D. A., and Mapes, B. E. (2007). Vertical-mode and cloud decomposition of large-scale convectively coupled gravity waves in a two-dimensional cloud-resolving model. *J. Atmos. Sci.*, 64(4):1210–1229.
- Walters, D., Boutle, I., Brooks, M., Thomas, M., Stratton, R., Vosper, S., Wells, H., Williams, K., Wood, N., Allen, T., et al. (2017). The met office unified model global atmosphere 6.0/6.1 and jules global land 6.0/6.1 configurations. *Geoscientific Model Development*, 10(4):1487.
- Wheeler, M. and Kiladis, G. N. (1999). Convectively coupled equatorial waves: Analysis of clouds and temperature in the wavenumber-frequency domain. *J. Atmos. Sci.*, 56(3):374–399.
- Yanai, M., Esbensen, S., and Chu, J.-H. (1973). Determination of bulk properties of tropical cloud clusters from large-scale heat and moisture budgets. *J. Atmos. Sci.*, 30(4):611–627.
- Zhang, F., Davis, C. A., Kaplan, M. L., and Koch, S. E. (2001). Wavelet analysis and the governing dynamics of a large-amplitude mesoscale gravity-wave event along the East Coast of the United States. *Quart. J. Roy. Meteor. Soc.*, 127(577):2209–2245.